micromachines

Article

Tackling Multi-Physics Nano-Scale Phenomena in Capillary Force Lithography with Small Data by Hybrid Intelligence

Ashish Chapagain and In Ho Cho *

Department of Civil, Construction, and Environmental Engineering, Iowa State University, Ames, IA 50011, USA; cashish@iastate.edu
* Correspondence: icho@iastate.edu

Abstract: The scientific community has been looking for novel approaches to develop nanostructures inspired by nature. However, due to the complicated processes involved, controlling the height of these nanostructures is challenging. Nanoscale capillary force lithography (CFL) is one way to use a photopolymer and alter its properties by exposing it to ultraviolet radiation. Nonetheless, the working mechanism of CFL is not fully understood due to a lack of enough information and first principles. One of these obscure behaviors is the sudden jump phenomenon—the sudden change in the height of the photopolymer depending on the UV exposure time and height of nano-grating (based on experimental data). This paper uses known physical principles alongside artificial intelligence to uncover the unknown physical principles responsible for the sudden jump phenomenon. The results showed promising results in identifying air diffusivity, dynamic viscosity, surface tension, and electric potential as the previously unknown physical principles that collectively explain the sudden jump phenomenon.

Keywords: nano capillary lithography; nano-grating; transparent machine learning; Bayesian evolutionary algorithm; hybrid intelligence

check for updates

Citation: Chapagain, A.; Cho, I.H. Tackling Multi-Physics Nano-Scale Phenomena in Capillary Force Lithography with Small Data by Hybrid Intelligence. *Micromachines* **2023**, *14*, 1984. https://doi.org/10.3390/mi14111984

Academic Editor: Aiqun Liu

Received: 5 October 2023
Revised: 23 October 2023
Accepted: 25 October 2023
Published: 26 October 2023

1. Introduction

Nanoscale structures are found commonly in nature and serve various essential functions. For instance, a chameleon's skin contains nanoscale crystals, which allows them to modify their appearance by adjusting their spacing. Learning from nature, modern progress in nanotechnology is geared towards harnessing the potential of nanotextures to perform a wide array of functions by manipulating the height of nano pixels [1–5]. Nanoscale capillary force lithography (CFL) is a nanofabrication technique that cures a photopolymer using UV radiation [6] to create patterns and structures on the nanoscale. CFL is gaining attention due to its high precision, potential for mass production, and relatively low cost. However, the physical principles at play are still obscure. One observed phenomenon in experiments is the sudden jump, where the height of the photopolymer experiences a rapid change at a specific UV dose (Figure 1c) [6].

Several research studies have been carried out in this sphere to explain the capillary behavior in nanochannels [7–10]. One intriguing phenomenon investigated is the Klingenberg effect [11] and its incorporation in gas flow through porous media [12–14]. One of the most recent advances involved discovering the hidden rules that explain the sudden jump phenomenon, with gas diffusivity, dynamic viscosity, and surface tension identified as the previously obscure physical principles governing this phenomenon [15]. However, it could not find the relationship between the height of the PDMS mold and its effect on the sudden jump. This paper has attempted to overcome this drawback and explain the sudden rise phenomenon for all heights of PDMS mold by combining physical principles alongside artificial intelligence, known as "hybrid intelligence". The hybrid intelligence approach is explained in Figure 1.

principles alongside artificial intelligence, known as "hybrid intelligence". The hybrid intelligence approach is explained in Figure 1.

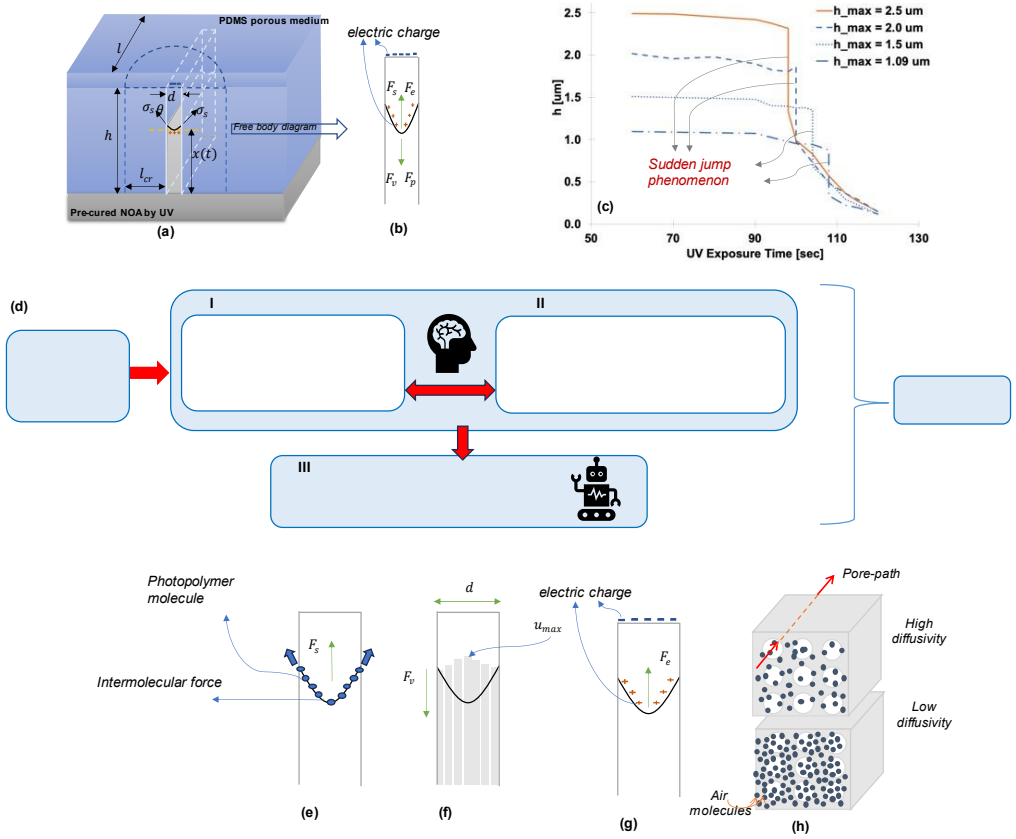

Figure 1. (**a**) Basic physics terms and geometrical properties of the capillary rising in a nano-grating and (**b**) their force equilibrium; (**c**) Height plots obtained from the rise of the same photopolymer into nano-grating with varying maximum heights. All cases commonly exhibit the sudden jump phenomena; (**d**) Architecture of the proposed hybrid intelligence approach. Step I includes the known parameters, which are included as input in our research. Step II consists of the known physical principles and their mathematical formulation. Steps I and II together make up human intelligence. Step III is the artificial intelligence, which includes a link function to identify the unknown physical phenomenon and Bayesian evolutionary algorithm; (**e**–**h**) Graphical representation of the recognized physical rules regarding surface tension (**e**), dynamic viscosity (**f**), electric (voltage) potential (**g**), and diffusivity of air molecules (**h**).

Current machine-learning (ML) approaches [16–18] show promising outcomes [19–21]. However, they are "black-box" models where the inner working of the model is not easily understandable or interpretable. Due to the inability of ML to unveil "transparent rules", this paper applies hybrid intelligence, used in [15], to explain the sudden jump phenomenon and its variation with PDMS height. Hybrid intelligence combines human and artificial intelligence to reveal the unknown physical rules (Figure 1d). On one hand, human intelligence draws upon fundamental physics, scientists' observation, experience, and knowledge. Unknown terms that are beyond current human understanding are included in the formulation. On the other hand, artificial intelligence provides the search capabilities to identify the most promising expressions for these unknown rules [15].

Although this paper has its beginnings in [15], considerable advances have been made since. There are significant differences between this paper and [15]. Firstly, this paper focuses on nano-grating geometry, while [15] deals with circular nanopillars. This distinction necessitates substantial adjustments in the formulation based on human intelligence. Secondly, this paper includes four different nano-grating heights, and we collectively employ all four experiments for rule learning. In contrast, ref. [15] conducted rule learning using just one nano-pillar experiment. Thirdly, this paper has made further advances to [15] by incorporating electric potential difference as an additional physical process involved in the

capillary rise in the nano-grating, thus requiring expansion of the previous three physics processes, i.e., dynamic viscosity, surface tension, and diffusivity [15].

This paper focuses on a few experiments (thus, small data) that commonly exhibit the complex sudden jump phenomena. The fundamental difficulty stems from the small length scale, time-varying salient properties (e.g., air pressure, air mass, diffusivity into porous medium, dynamic viscosity, surface tension, and electric potential-dependent forces), and the multi-physical phenomenon interactions during the nano capillary rising. Obtaining large data sets is often difficult and expensive. Sometimes, internal data are intrinsically inaccessible due to technological limitations such as the inability to monitor the liquid's behavior inside the nano-ridge during the capillary rise and to precisely measure the electric charge inside the nano-ridge.

In our study, we observed four key phenomena that collectively contribute to the explanation of the sudden jump phenomenon:

- Air diffusivity decreases as the rate of trapped air-mass transfer increases;
- The dynamic viscosity of the liquid increases upon exposure to UV radiation;
- Our results demonstrate that UV exposure leads to a reduction in the surface tension of the liquid;
- The electric potential between the liquid and the PDMS mold decreases as the distance between the liquid's top surface and the bottom surface of the PDMS mold increases.

These observed phenomena collectively contribute to our understanding of the sudden jump phenomenon, shedding light on the underlying physical principles at play in this intriguing phenomenon.

2. Materials and Methods

2.1. Data Preparation

We assessed the topography of the printed nano-ridge array using atomic force microscopy (AFM) in tapping mode, employing highly doped silicon tips (NCHR, NanoWorld, Neuchâtel, Switzerland). Comprehensive details regarding nanofabrication procedures and AFM data acquisition are outside the scope of this paper and will be the subject of a dedicated future publication. It should be noted that the total data points are artificially increased for smooth training using interpolation when the trend drastically changes, such as near the sudden jump region. Such regions show infinite slopes, which may cause mathematical issues and difficulty fitting with smooth LFs (Figure 1c). For instance, in the 1.5 μm case, two points (x, y) = (15,600, 1.35) and (15,600, 0.679) showing the infinite slope may be refined to five points (non-infinite slope) with additional points at (x, y) = (15,500, 1.35), (15,550, 1.18), (15,600, 1.0155), (15,650, 0.847), and (15,700, 0.679) using interpolation. Since a simple interpolation generates the increased data points, the overall shape of the experimental values does not change. All experimental data will be made available upon request to the author.

2.2. Two Pillars of the Hybrid Intelligence—Human and Artificial Intelligences

2.2.1. Human Intelligence for Providing Basic Formulations with Basic Physics Quantities

The mathematical formulation used in this study is derived mainly from [15]. The formulation that relates the PDMS mold's height with sudden jump—the potential (voltage) difference—is shown in the succeeding section. This section provides a comprehensive formulation and terminology governing the principles of force equilibrium and mass balance in the context of nano capillary rise.

1. Force equilibrium formulation

The ascent of a fluid within a vertical nano-ridge is determined using an interplay of multiple force components, which can be expressed as follows: $F_s - F_v - F_P - F_g + F_e = 0$. Here, F_s denotes the capillary force driven by the liquid's surface tension, F_v is the viscous force that counteracts the liquid's rise, F_P is the force due to air pressure confined within the nano-ridge [15], and F_g is the gravitational force. A new force term is introduced into the

The ascent of a fluid within a vertical nano-ridge is determined using an interplay of multiple force components, which can be expressed as follows: $F_s - F_v - F_P - F_g + F_e = 0$. Here, F_s denotes the capillary force driven by the liquid's surface tension, F_v is the viscous force that counteracts the liquid's rise, F_P is the force due to air pressure confined within the nano-ridge [15], and F_g is the gravitational force. A new force term is introduced into the formulation by [15], F_e, which characterizes the electric potential-dependent force. Figure 2 illustrates the liquid's height $x(t)$ at time t. The individual force components are defined as $F_s = 2l\sigma_s cos(\theta)$, $F_v = 12lx(t)\frac{\mu}{d}\frac{\delta x}{\delta t}$ [22], and $F_g = d \cdot l \cdot x(t) \cdot \rho g$, which are described in [23]. For the electric potential, we considered the pressure caused by the electric force, denoted as p_e, which is described in [23]. The exact formulation is given by: $p_e = \frac{1}{2}\epsilon_0\left(\frac{1}{\epsilon_1} - \frac{1}{\epsilon_2}\right)\left[\frac{\epsilon_1\epsilon_2 U}{\epsilon_1 h + \epsilon_2(d-h)}\right]^2$. Here, ϵ_0 is the permittivity of a vacuum, ϵ_1 is the dielectric constant of air, ϵ_2 is the dielectric constant of the liquid, and U represents the applied potential difference. From this equation, it is evident that the pressure is directly proportional to the square of potential difference ($p_e \propto U^2$) and inversely proportional to the square of $(d-h)$ ($p_e \propto \frac{1}{(d-h)^2}$). However, U, ϵ_0, ϵ_1, and ϵ_2 are unknown quantities. As a result, we introduce a term, $U(h)$, which collectively accounts for the influence of these four variables. This leads to the establishment of the simplified expression for p_e as $p_e = \frac{U(h)}{(d-h)^2}$. So, F_e is the area on which the pressure exerts times the pressure force. Therefore, $F_e = \frac{d \cdot l \cdot U(h)}{(h-x(t))^2}$, where all the unknown terms are contained in $U(h)$, which will be learned by machine learning later. While we did not consider curvature for electric forces in this study, we agree that it is an important factor. We plan to include it in our future research to increase accuracy. Here, l is the length of the nano-ridge, $\sigma(U_v)$ [N/m] is the surface tension of the liquid (initial value = 0.04 N/m) which depends on the total UV dose (U_v) [$\frac{J}{m^2}$], θ [deg] is the contact angle between the liquid and the nano-ridge (75 degrees), $\mu(U_v)$ [$\frac{Ns}{m^2}$] is the U_v-dependent dynamic viscosity of the liquid (initial value = 0.4 $\frac{Ns}{m^2}$), $\frac{dx}{dt}$ is the average velocity of the rise of the liquid, d is the distance between two walls of the nano-ridge (1500 nm), $P(t)$ [$\frac{N}{m^2}$] is the pressure of air confined in the nano-ridge at time t, $P(0)$, the initial air pressure, is assumed to be the atmospheric pressure (101,325 Pa), and g is the acceleration due to gravity. It is worth noting that the gravitational force is substantially smaller in magnitude compared to the other terms, rendering it negligible in the subsequent consideration. We arrive at the following expression upon incorporating all these force components into the equilibrium equation. It needs to be noted that while the formulation method is similar to [15], the following formulation differs in the geometry and inclusion of the electric force.

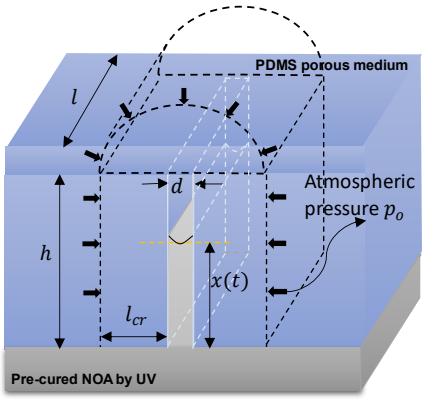

Figure 2. 3D view of a single nano-ridge with pressure boundary conditions and geometry.

$$2l\sigma_s cos(\theta) - 12lx(t)\frac{\mu}{d}\frac{\delta x}{\delta t} - d \cdot l \cdot (P(t) - P(0)) + \frac{d \cdot l \cdot U(h)}{(h - x(t))^2} = 0. \quad (1)$$

Applying the ideal gas law to the air confined within the pressure term can be expressed in the following manner: $P(t) = \frac{m(t)}{Mdl(h-x(t))}RT$ and $P(0) = \frac{m(0)}{Mdlh}RT$, where $m(t)$ [kg] is the mass of confined air at time t, R is the universal gas constant (8.3144 J/mol/K), T [K] is the absolute temperature (78 K), and M [kg/mol] is the molar mass of the confined

air (0.02897 kg/mol). Substituting the pressure expressions into the equilibrium equation, we can derive the equation governing the velocity of the liquid's ascent as follows:

$$\frac{\delta x}{\delta t} = \frac{\sigma(U_v)dcos(\theta)}{6\mu(U_v)x(t)} - \frac{RTd}{12\mu(U_v)lMx(t)}\left(\frac{m(t)}{h-x(t)} - \frac{m(0)}{h}\right) + \frac{d^2U(h)}{12\mu(U_v)x(t)(h-x(t))^2} \quad (2)$$

where $m(t)$ is the mass of trapped gas at time t, h is the total height of the capillary (1090 nm, 1500 nm, 2000 nm, and 2500 nm), $m(0)$ is the initial mass of the trapped gas, and $U(h)$ is a link function to account for the voltage (potential) difference and dielectric constants, which will be learned by the proposed machine-learning method.

The time required for the liquid to rise to height (h) when the nano-ridge is open-ended (i.e., no cap) can derived by t_{rise}=$\int_0^h \left(\frac{dx}{dt}\right)^{-1} ds = \frac{3\mu h^2}{\sigma dcos(\theta)}$ [15].

2. Mass balance formulation

As air is trapped within the nano-ridge, it will gradually decrease due to diffusion into nanopores within the PDMS mold. To establish the rate of change of mass of the trapped gas, we can derive it from the mass balance equation as follows [15]:

$$\frac{\delta m}{\delta t} = \frac{-D_d K_H A(t)}{l_{cr}} \frac{RT}{d \cdot l}\left(\frac{m(t)}{h-x(t)} - \frac{m(0)}{h}\right) \quad (3)$$

where D_d is the coefficient of diffusion, K_H is Henry's constant, $A(t) = d \cdot l + 2l(h - x(t))$ is the area through which diffusion takes place, and the distance at which the air pressure diffuses is taken as l_{cr}. Here , l_{cr} is the nanopore pressure critical length [m] measured from the nano-ridge's wall. At l_{cr}, the internal pore pressure becomes $p_0 = P(0)$ (Figure 2). In this work l_{cr} is assumed to be constant at $10h$. $D_K\left(\frac{d\overline{m}}{d\overline{t}}\right) \equiv D_d K_H$ is a function of the air mass flux rate whose initial value is 1×10^{-12} mol·s/kg. D_d is the diffusion coefficient of the air into PDMS pores. This study posits that a sudden surge in airflow into PDMS nanopores can impede air diffusion within these nanopores, much like a traffic jam can be caused by a sudden increase in traffic volume at a fixed intersection. Figure 1h illustrates this physical rationale schematically. Obtaining accurate time-varying models for D_d and K_H separately can be challenging. Therefore, this study employs a glass-box approach to identify the combined effect of D_d and K_H, represented as D_K. The rise in height, mass, and time are normalized as

$$\overline{x}(\overline{t}) = \frac{x(t)}{h};\ \overline{m}(\overline{t}) = \frac{m\ (t)}{m(0)};\ \overline{t} = \frac{t}{t_{rise}}. \quad (4)$$

Thus, normalized force equilibrium and mass balance equations are given as

$$\frac{\delta \overline{x}}{\delta \overline{t}} = \frac{1}{2\overline{x}(\overline{t})} - \frac{\alpha}{2}\left(\frac{\overline{m}(\overline{t}) - 1 + \overline{x}(\overline{t})}{\overline{x}(\overline{t})\left(1 - \overline{x}(\overline{t})\right)}\right) + \frac{\gamma}{\overline{x}(\overline{t})\left(1 - \overline{x}(\overline{t})\right)^2} \quad (5)$$

and

$$\frac{\delta \overline{m}}{\delta \overline{t}} = -\beta\left(1 + \frac{2h}{d}\left(1 - \overline{x}(\overline{t})\right)\right)\left(\frac{\overline{m}(\overline{t}) - 1 + \overline{x}(\overline{t})}{\left(1 - \overline{x}(\overline{t})\right)}\right). \quad (6)$$

To simplify and condense the equations above, we introduce additional coefficients α, β, and γ. Here, $\alpha = \frac{P(0)d}{2\sigma cos(\theta)}$, $\beta = \frac{3\mu D_d K_H RTh}{d\sigma cos(\theta) l_{cr}}$, $\gamma = \frac{U(h)d}{4\sigma h^2 cos(\theta)}$, and $D_d K_H$ is a function of $\frac{\delta \overline{m}}{\delta \overline{t}}$.

To this point, human intelligence mathematically formulates the liquid rise velocity and the mass rate in the presence of physics quantities. But they are not complete. Those physics-driven formulations inevitably contain several unknown terms, of which rules need to be tackled by artificial intelligence, as described in the following section. The physical

phenomena under consideration and the corresponding link functions are summarized in Table 1.

Table 1. Summary of physical phenomena and the LF used to identify them.

Unknown Physics Term	Function Argument	Physical Meaning	Best Identified LF
$D_d K_H$	$\frac{d\overline{m}}{d\overline{t}}$	Diffusivity of trapped air into PDMS pores	2-parameter exponential function $(\exp(c_1 x^{c_2}))$
μ	$\overline{U_V}$	Dynamic viscosity of the liquid	2-parameter exponential function $(\exp(c_1 x^{c_2}))$
σ	$\overline{U_V}$	Surface tension of the liquid	2-parameter exponential function $(\exp(c_1 x^{c_2}))$
U	$\overline{h}$	Potential (voltage) difference between the lower surface of PDMS and the upper surface of the liquid and dielectric constants of the materials	3-parameter 2nd-order polynomial function $(c_1 x^2 + c_2 x + c_3)$

2.2.2. Artificial Intelligence for Exploring and Searching Hidden Rules

1. Flexible link functions

The search for transparent link functions (LFs) is conducted using the Bayesian evolutionary algorithm. For the effective utilization of LF ($\mathcal{L}$), the input arguments have been normalized to the range [0, 1]. As in [15], the relationship between the UV dose and the terms σ and μ is related as $\sigma(U_v) = \sigma_0 \mathcal{L}_\sigma(\overline{U_v}; \theta_\sigma)$ and $\mu(U_v) = \mu_0 \mathcal{L}_\mu(\overline{U_v}; \theta_\mu)$, where σ_0 and μ_0 are the surface tension and the dynamic viscosity of the liquid in the absence of UV exposure, respectively. The UV dose is normalized as $\overline{U_v} = U_v/36,000\ \left[\mathrm{J/m^2}\right] \in \mathbb{R}[0,1)$. θ is the free parameter vector, which is learned using the Bayesian algorithm. The initial values of $\sigma_0 = 0.04$ N/m and $\mu_0 = 0.4$ N·s/m^2 is assumed for the study. The function $D_K\left(\frac{d\overline{m}}{d\overline{t}}\right) = D_{K0}\mathcal{L}_{D_K}\left(\max_{\forall t}\left[\frac{d\overline{m}}{d\overline{t}}\right]; \theta_{D_K}\right)$ is used to describe the maximum flux rate over time, where D_{K0} is the initial value of $D_d K_H$, and this study assumed $D_d K_H = 1 \times 10^{-12}$.

A relationship between the normalized height of grating ($\overline{h}$) and the physics term U will be related by function as $U\left(\overline{h}\right) = U_0 \mathcal{L}_U\left(\overline{h}; \boldsymbol{\theta}_U\right)$, where $\overline{h}$ is normalized as $\frac{h}{10^{-6}}$. In this study, the initial value of U_0 is assumed 2×10^{-8}. $\mathcal{L}_U$ is a link function used to account for the potential (voltage) difference and dielectric constants.

A general two-parameter exponential LF [24–28], i.e., two-parameter exponential LF with the form $\mathcal{L}(x) = \exp(c_1 x^{c_2})$, was chosen (Figure 3) for surface tension, dynamic viscosity, and diffusivity of air. To include the effect of electric force based on [23], a second-order polynomial LF of the form $\mathcal{L}(x) = c_1 x^2 + c_2 x + c_3$ was chosen among a few choices. The rationale for this selection of the LF is presented in the discussion section later.

2. Bayesian evolutionary algorithm

This paper has employed a fusion of the genetic algorithm's fitness-proportionate probability (FPP) rule and the Bayesian update scheme to ensure seamless rule learning. Following the FPP rule, the likelihood of an organism (denoted as "o") from the present generation being chosen for the subsequent generation is directly related to its fitness score ($\mathcal{F}$) where organism "o" is a distinct manifestation of free parameters $\left(\boldsymbol{\Theta} = \left\{\boldsymbol{\theta}_1, \ldots, \boldsymbol{\theta}_{n_{rule}}\right\}\right)$ within all concealed rules. The fitness score ($\mathcal{F}$) is given by $\mathcal{F}(s) = (1 + Err(s))^{-1}$ where $Err(s) = n^{-1}\sum_i^n \frac{\left(x_{real}^{(i)} - x_{pred}^{(i)}\right)^2}{\left(x_{real}^{(i)}\right)^2}$. A reduced error corresponds to increased fitness. The fitness score of the previous best generation and the collection of all the free parameter sets $\boldsymbol{\Theta}$ from the same generation are represented as $\mathcal{F}^*(o)$ and $O^*(\boldsymbol{\Theta})$, respectively. Since each $\boldsymbol{\Theta}$ can be uniquely represented by an organism, the interchangeability of organism and $\boldsymbol{\Theta}$ is established: $p(o) \propto \mathcal{F}(o)$, equivalently $p(\boldsymbol{\Theta}) \propto \mathcal{F}(o)$. Subsequently, the Bayesian

Micromachines **2023**, *14*, x FOR PEER REVIEW 7 of 16

fitness score of a novel individual organism (denoted as $\mathcal{F}_B(o)$) is formulated as $\mathcal{F}_B(o) = \frac{1}{\kappa}\frac{\mathcal{F}(o;O^*(\boldsymbol{\Theta}))\mathcal{F}^*(o)}{\sum_{\forall o}\mathcal{F}^*(o)}$ where $\kappa = \sum_{\forall o}\frac{\mathcal{F}(o;O^*(\boldsymbol{\Theta}))\mathcal{F}^*(o)}{\sum_{\forall o}\mathcal{F}^*(o)}$ is a normalization term. The probability of parent selection for the upcoming generation is denoted as $p(parent_i \mid o) \propto \mathcal{F}_B(o), (i = 1,2)$. Consequently, all the identified LFs can seamlessly evolve with new experimental data. Within the Bayesian evolutionary framework, a cumulative count of 100,000 organisms and 10 generations are employed, encompassing four alleles for every gene. The mutation mechanism operates per-variable, with a mutation rate of 0.005.

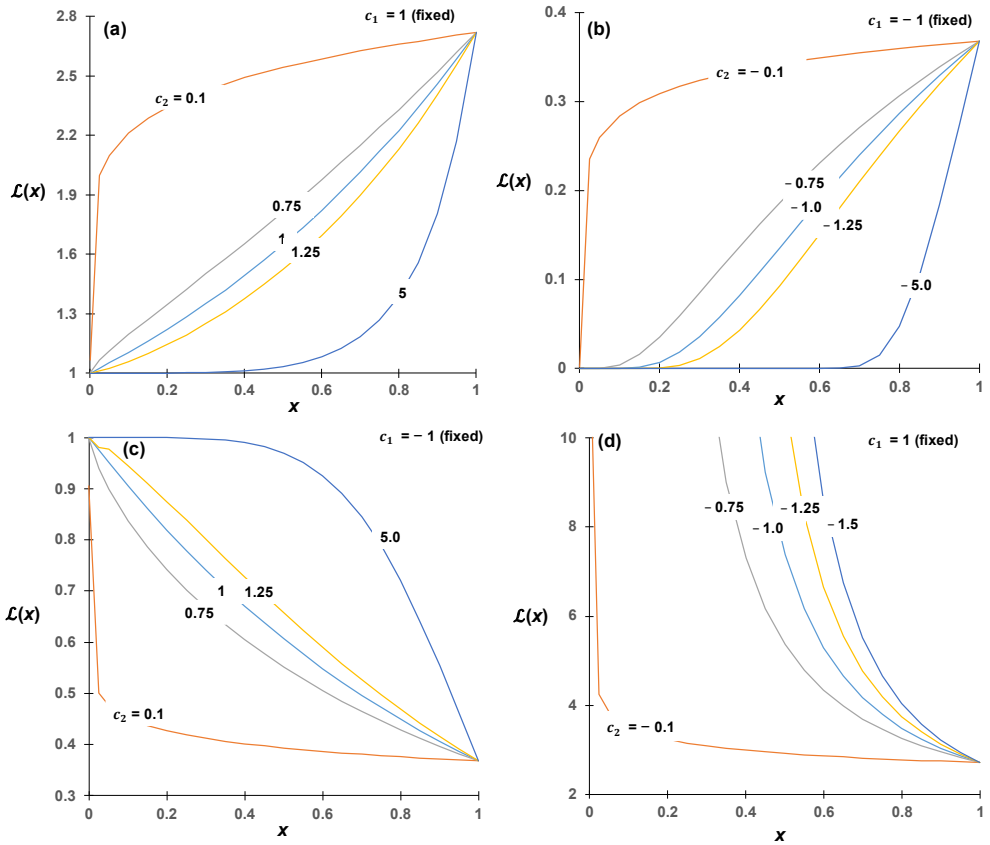

Figure 3. Example plots of the two-parameter exponential link function: general nonlinear increasing relations (**a**,**b**) and decreasing relations (**c**,**d**) where $\mathcal{L}(x) = \exp(c_1 x^{c_2})$.

2. Bayesian evolutionary algorithm

This paper has employed a fusion of the genetic algorithm's fitness-proportionate probability (FPP) rule and the Bayesian update scheme to ensure seamless rule learning. Following the FPP rule, the likelihood of an organism (denoted as "o") from the present generation being chosen for the subsequent generation is directly related to its fitness score, $(\mathcal{F}_S)$, where organism "o" is a distinct manifestation of free parameters $(\boldsymbol{\theta} = \{\theta_1, \ldots, \theta_{|\boldsymbol{\theta}|}\})$ within all concealed rules. The fitness score $(\mathcal{F})$ is given by $\mathcal{F}(s) = (1 + Err(s))^{-1}$, where $Err(s) = n^{-1}\sum_n^{(i)}\frac{(x_{real}^{(i)} - x_{pred}^{(i)})^2}{(x_{real}^{(i)})^2}$. A reduced error corresponds to increased fitness. The fitness score of the previous best generation and the collection of all the free parameter sets $\boldsymbol{\Theta}$ from the same generation are represented as $\mathcal{F}^*(o)$ and $O^*(\boldsymbol{\Theta})$, respectively. Since each $\boldsymbol{\Theta}$ can be uniquely represented by an organism, the interchangeability of organism and $\boldsymbol{\Theta}$ is established: $p(o) \propto \mathcal{F}(o)$, equivalently $p(\boldsymbol{\theta}) \propto \mathcal{F}(o)$. Subsequently, the Bayesian fitness score of a novel individual organism (denoted as $\mathcal{F}_B(o)$) is formulated as $\mathcal{F}_B(o) = \frac{1}{\kappa}\frac{\mathcal{F}(o;O^*(\boldsymbol{\Theta}))\mathcal{F}^*(o)}{\sum_{\forall o}\mathcal{F}^*(o)}$ where $\kappa = \sum_{\forall o}\frac{\mathcal{F}(o;O^*(\boldsymbol{\Theta}))\mathcal{F}^*(o)}{\sum_{\forall o}\mathcal{F}^*(o)}$ is a normalization term. The probability of parent selection for the upcoming generation is denoted as $p(parent_i \mid o) \propto \mathcal{F}_B(o), (i = 1,2)$. Consequently, all the identified LFs can seamlessly evolve with new experimental data. Within the Bayesian evolutionary framework, a cumulative count of 100,000 organisms and 10 generations are employed, encompassing four alleles for every gene. The mutation mechanism operates per-variable,

We can anticipate whether $\mathcal{L}(x)$ will rise or fall using human intelligence. Figure 3 provides us with cues to deduce the signs of c_1 and c_2. Subsequently, we initiated our exploration within a broad interval. In our specific case, the initial ranges for c_1, c_2, and c_3 were set to a wide search range (ranging from −10 to +10). During the training process, we progressively narrowed down our search ranges using a technique known as the shrinking search range method, ultimately establishing our final search ranges. Therefore, hybrid intelligence found the best-performing search ranges $c_1 \in [-8, -6]$ and $c_2 \in [0, 10]$ for LFs of diffusivity, $c_1 \in [8, 10]$ and $c_2 \in [0, 10]$ for LFs of dynamic viscosity, $c_1 \in [-6, -4]$ and $c_2 \in [0, -10]$ for LFs of surface tension, and for LF of potential (voltage) difference, $c_1 \in [0, 0.15]$, $c_2 \in [-0.4, 0]$, and $c_3 \in [0, 1.3]$.

The model was trained using the Bayesian update, which updates free parameters $(\boldsymbol{\Theta})$ with each experimental case, subsequently following the order presented in Figure 4. In our model, we set $n_{test} = 4$ and $n_{epoch} = 10$. An epoch concluded after processing the 2.5 case, at which point the 1.09 case experimental data was reintroduced for further training. This process is iterated for up to 10 epochs. The model's accuracy increases with more training epochs (Figure 5), but after the fifth epoch, accuracy appears to reach a plateau. Thus, this paper presents the best-so-far rules obtained after the fifth epoch of Bayesian evolutions.

more training epochs (Figure 5), but after the fifth epoch, accuracy appea
plateau. Thus, this paper presents the best-so-far rules obtained after the
Bayesian evolutions.

more training epochs (Figure 5), but after the fifth epoch, accuracy appears to reach a plateau. Thus, this paper presents the best-so-far rules obtained after the fifth epoch of Bayesian evolutions.

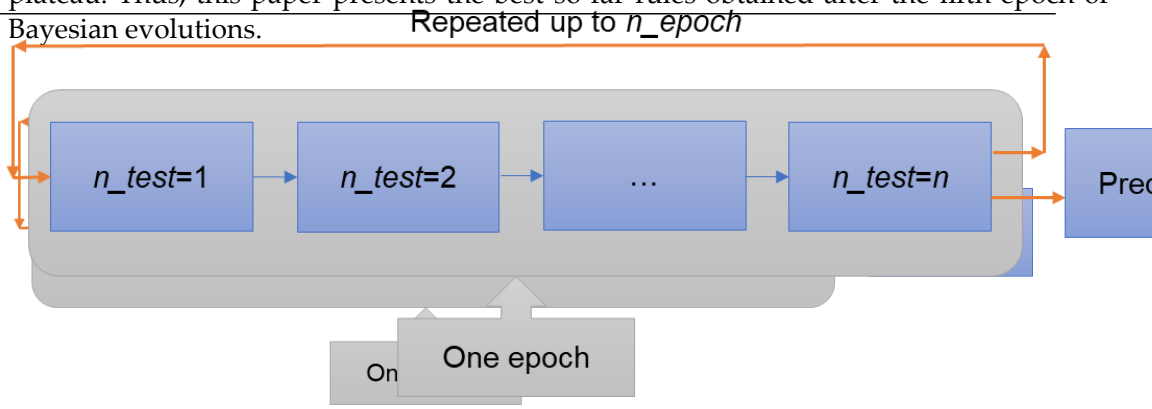

Figure 4. Bayesian evolutionary training sequences with multiple experiments.

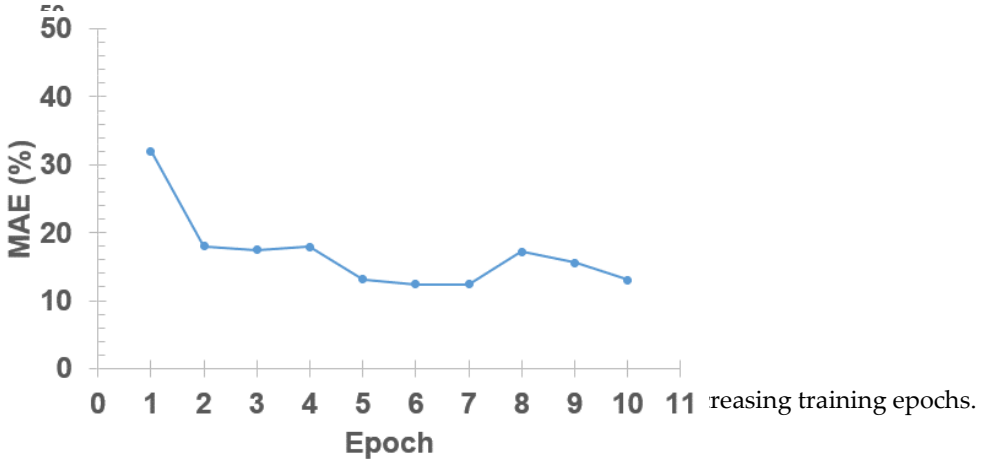

reasing training epochs.

2.3. Feasibility Test Result

Figure 5. Accuracy variations of the Bayesian evolution with increasing training epo

The experiment consisted of four cases depending on the height of the grating. The heights were 1.09 µm, 1.5 µm, 2.0 µm, and 2.5 µm. The corresponding experiments are named the 1.09 case, 1.5 case, 2.0 case, and 2.5 case, respectively. Figure 6a–d compare experimental results of the nano capillary rising heights and reproductions with the best-so-far rules identified by the proposed hybrid intelligence approach. At the sudden change in the height near the total UV dose (15,000–17,000 J/m²), we conducted AFM analyses on the samples right above and below the sudden jump for more comparisons. Applying the glass-box ML-identified rules, the final heights above and below the sudden jump were well reproduced (Figure 6a–d). Figure 6a–d reproduce the normalized height with increasing UV dose. The normalized height is the final height of liquid scaled down to a range of [0, 1] by $\frac{x(t)}{h}$. For instance, in the 1.09 case, normalized height = 1 means that the liquid has reached the final height of 1.09 µm.

named the 1.09 case, 1.5 case, 2.0 case, and 2.5 case, respectively. Figure 6 experimental results of the nano capillary rising heights and reproductions so-far rules identified by the proposed hybrid intelligence approach. A change in the height near the total UV dose (15,000–17,000 J/m²), we co analyses on the samples right above and below the sudden jump for mor comparisons. Applying the glass-box ML-identified rules, the final heigh below the sudden jump were well reproduced (Figure 6a–d). Figure 6a–d r normalized height with increasing UV dose. The normalized height is the f liquid scaled down to a range of [0, 1] by $\frac{x(t)}{h}$. For instance, in the 1.09 cas height = 1 means that the liquid has reached the final height of 1.09 µm.

Figure 7 shows how the proposed hybrid intelligence approach improves the rise using the top 10 best-so-far rules for the four cases, respectively. This plot shows the uncertainty levels of the best-so-far rules' prediction.

The transparent window-type optical rules (Figure 8) are, instead, about the dynamic viscosity (Figure 8b) and surface tension (Figure 8c) of the photopolymer (NOA73) as nonlinear functions of the total UV doses; a rule about the air diffusivity (Figure 8a) as a nonlinear function of air mass flux rate into the nanopores in the mold made of PDMS; and a rule about the electric potential difference (Figure 8d).

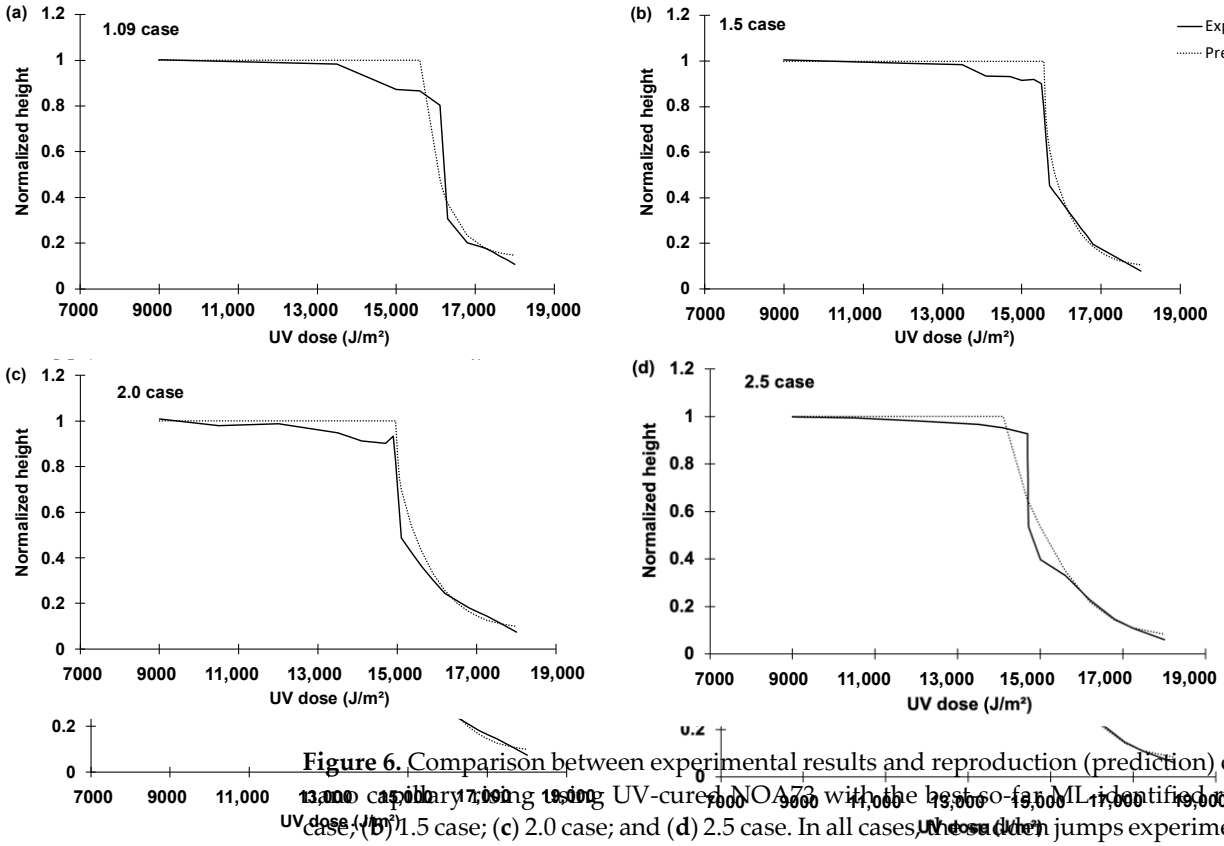

Figure 6. Comparison between experimental results and reproduction (prediction) of final height of nano-capillary rising using UV-cured NOA73 with the best-so-far ML-identified rules for: (**a**) 1.09 case; (**b**) 1.5 case; (**c**) 2.0 case; and (**d**) 2.5 case. In all cases, the sudden jumps experimentally observed near 15,000 ~17,000 J/m^2 are well captured by the transparent ML-identified rules.

Figure 6. Comparison between experimental results and reproduction (prediction) of final height of nano-capillary rising using UV-cured NOA73 with the best-so-far ML-identified rules for: (**a**) 1.09 case; (**b**) 1.5 case; (**c**) 2.0 case; and (**d**) 2.5 case. In all cases, the sudden jumps experimentally observed near 15,000 ~17,000 J/m^2 are well captured by the transparent ML-identified rules.

Figure 7a–d show the mean and one-standard range of the reproduction of the liquid rise using the top 10 best-so-far rules for the four cases, respectively. This plot shows the uncertainty levels of the best-so-far rules' prediction.

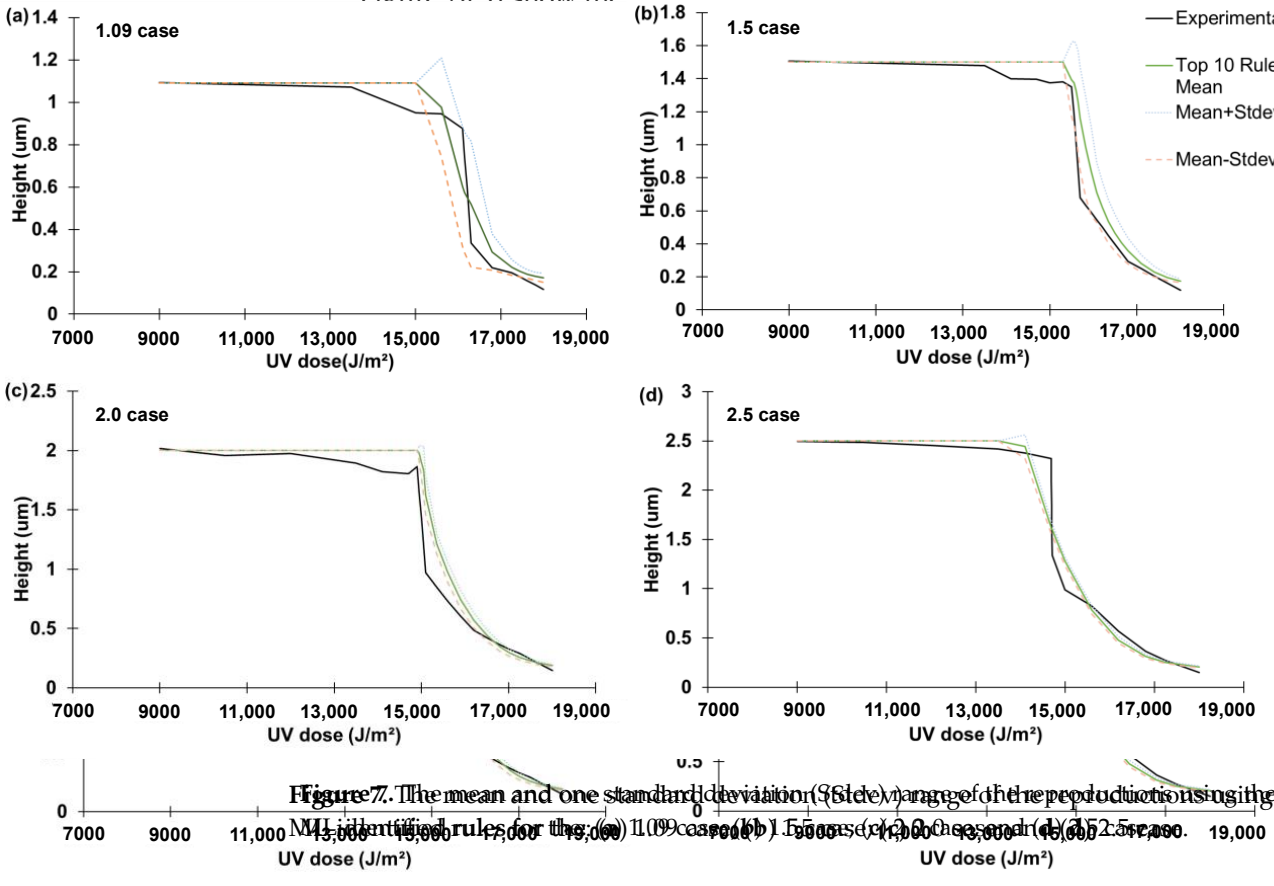

Figure 7. The mean and one standard deviation (Stdev) range of the reproductions using the top 10 ML-identified rules for the: (**a**) 1.09 case; (**b**) 1.5 case; (**c**) 2.0 case; and (**d**) 2.5 case.

Figure 7. The mean and one standard deviation (Stdev) range of the reproductions using the top 10 ML-identified rules for the: (**a**) 1.09 case; (**b**) 1.5 case; (**c**) 2.0 case; and (**d**) 2.5 case.

The transparent ML sought to learn four hidden rules (Figure 8)—i.e., two rules about the dynamic viscosity (Figure 8b) and surface tension (Figure 8c) of the photopolymer (NOA73) as nonlinear functions of the total UV doses; a rule about the air diffusivity (Figure 8a) as a nonlinear function of air mass flux rate into the nanopores in the mold made of PDMS; and a rule about the electric potential difference (Figure 8d).

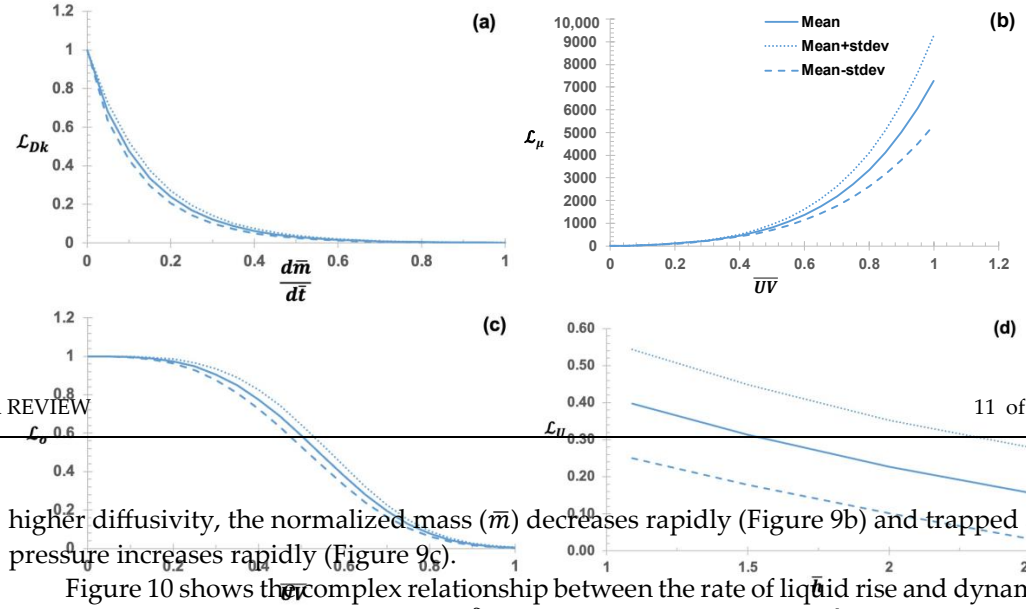

Figure 8. (**a**) Identified link function (LF) of diffusivity of air molecules passing through the PDMS nanopores, $\mathcal{L}_{D_K}(\frac{d\bar{m}}{d\bar{t}}; \boldsymbol{\theta}_{D_K})$, as a function of the normalized air mass flux rate ($d\bar{m}/d\bar{t}$); (**b**) LF of the dynamic viscosity of NOA73 (pre-cured by UV), $\mathcal{L}_{\mu}(\bar{U}_v; \boldsymbol{\theta}_{\mu})$, as a function of the normalized UV dose ($\bar{U}_v$); (**c**) LF of the surface tension of NOA73, pre-cured by U.UV, $\mathcal{L}_{\sigma}(\bar{U}_v; \boldsymbol{\theta}_{\sigma})$; (**d**) LF of the potential (voltage) difference between the top surface of NOA73 and the lower surface of the PDMS template, $\mathcal{L}_U(\bar{U}; \boldsymbol{\theta}_U)$ as a function of the normalized height of the top PDMS template. The faded lines show a one-sta

higher diffusivity, the normalized mass ($\bar{m}$) decreases rapidly (Figure 9b) and trapped air pressure increases rapidly (Figure 9c).

Figure 10 shows the complex relationship between the rate of liquid rise and dynamic viscosity (μ). Equation (6) shows that $\frac{\delta\bar{m}}{\delta\bar{t}} \propto -\beta$, where $\beta = \frac{3\mu D_d K_H RTh}{d\sigma\cos(\theta)l_{cr}}$. This leads to $\frac{\delta\bar{m}}{\delta\bar{t}} \propto \frac{1}{\mu}$. The second term of the equation, $\frac{\delta\bar{x}}{\delta\bar{t}}$, is a function of $\bar{x}$, which can be found in Equation (10). Consequently, $\frac{\delta\bar{m}}{\delta\bar{t}} \propto \frac{1}{\mu}$, which means that as the dynamic viscosity increases, the rate of liquid rise decreases, and vice versa. This is also evident in Figure 10, where the liquid rises faster for lower dynamic viscosity ($\mu = 0.004$ Ns/m^2) and slower for higher dynamic viscosity ($\mu = 0.04$ Ns/m^2). The nonlinear relationship between the liquid rise and dynamic viscosity is also evident in Figure 10, where the rate of liquid rise is not linear. Figure 11 shows that as the surface tension increases, the rate of liquid rise also increases, but the trend is nonlinear. The initial electric potential appears to accelerate the liquid rise, but the trend is nonlinear (Figure 12). The normalized height ($\bar{x}$) is the representation of the liquid rise scaled between the range [0, 1] given by $\bar{x} = \frac{x(t)}{x_{max}}$, where $\bar{x} = 1$ means the liquid has attained its maximum height. Similarly, normalized mass ($\bar{m}$) is the mass of trapped air scaled between the range [0, 1] given by $\bar{m} = \frac{m(t)}{m(0)}$. $\bar{m} = 1$ signifies that no trapped air has escaped the capillary, and conversely, $\bar{m} = 0$ signifies that all the trapped air has escaped through the PDMS pores. And normalized pressure ($\bar{p}$) = 1 signifies the actual pressure of the trapped air equal to the atmospheric pressure. Equation (5) it becomes evident that $\frac{\delta\bar{m}}{\delta\bar{t}} \propto \gamma$, where $\gamma = \frac{1}{\sigma}$ signifies that the value of $U(t)$ has increased, the rate of liquid rise also increases, leading to the required attainment of the liquid's maximum height. Apparent pressure (Figure 9a). This is aligned with basic physics, i.e., the higher the diffusivity, the faster the trapped air escapes. Similarly, with

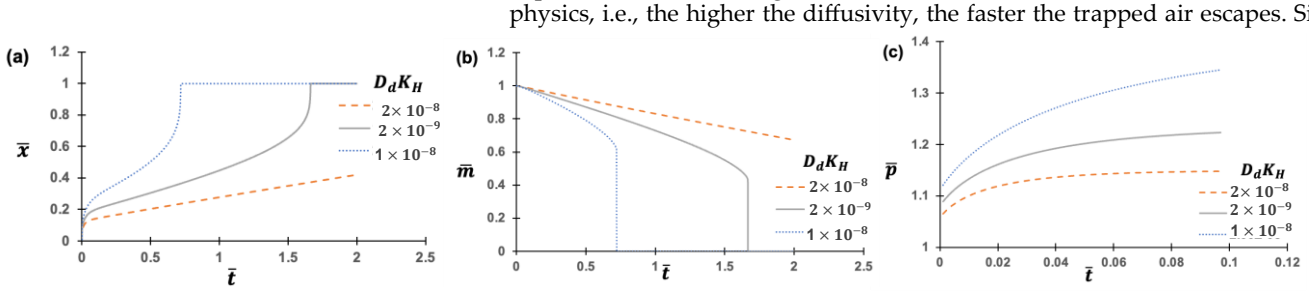

Figure 9. Parametric study of the impact of air diffusivity D_dK_H [mol·s/kg]: (**a**) Normalized liquid height; (**b**) Normalized air mass; (**c**) Normalized air pressure. Other parameters are fixed, the dynamic viscosity $\mu = 0.4$ Ns/m^2, the surface tension $\sigma = 0.04$ N/m, and $U_0 = 1 \times 10^{-8}$.

Figure 8. (**a**) Identified link function (LF) of diffusivity of air molecules passing through the PDMS nanopores, $\mathcal{L}_{D_K}(\frac{d\bar{m}}{d\bar{t}}; \boldsymbol{\theta}_{D_K})$, as a function of the normalized air mass flux rate ($d\bar{m}/d\bar{t}$); (**b**) LF of the dynamic viscosity of NOA73 (pre-cured by UV), $\mathcal{L}_{\mu}(\bar{U}_v; \boldsymbol{\theta}_{\mu})$, as a function of the normalized UV dose ($\bar{U}_v$); (**c**) LF of the surface tension of NOA73, pre-cured by U.UV, $\mathcal{L}_{\sigma}(\bar{U}_v; \boldsymbol{\theta}_{\sigma})$; (**d**) LF of the potential (voltage) difference between the top surface of NOA73 and the lower surface of the PDMS template, $\mathcal{L}_U(\bar{U}; \boldsymbol{\theta}_U)$ as a function of the normalized height of the top PDMS template. The faded lines show a one-standard deviation range (i.e., $\pm\sigma$) of the top 10 best-so-far rules.

3. Discussion

3.1. Parametric Study

We conducted parametric studies to understand the impact of the salient physics parameters (i.e., initial values of the air diffusivity D_dK_H (Figure 9), the dynamic viscosity μ (Figure 10), the surface tension σ (Figure 11), and the initial potential (voltage) difference (Figure 12)) on the rate of liquid rise, specifically, as surface tension increases, the time required for the liquid to attain its maximum height increases. The rate of liquid rise, however, is nonlinear. Figure 12 shows that the rate of liquid rise and the potential (voltage) difference (U) are directly proportional to each other. A potential difference existing between the lower surface of the PDMS template and the top surface of NOA73 (Figure 4) causes the liquid to rise between them. Consequently, U actively contributes to the rate of liquid rise. Following Equation (5), it becomes evident that $\frac{\delta\bar{m}}{\delta\bar{t}} \propto \gamma$, where $\gamma = \frac{1}{\sigma}$ signifies that the value of $U(t)$ has increased, the rate of liquid rise also increases, leading to the required attainment of the liquid's maximum height. Apparent pressure

Figure 9. Parametric study of the impact of air diffusivity D_dK_H [mol·s/kg]: (**a**) Normalized liquid height; (**b**) Normalized air mass; (**c**) Normalized air pressure. Other parameters are fixed, the dynamic viscosity $\mu = 0.4$ Ns/m^2, the surface tension $\sigma = 0.04$ N/m, and $U_0 = 1 \times 10^{-8}$.

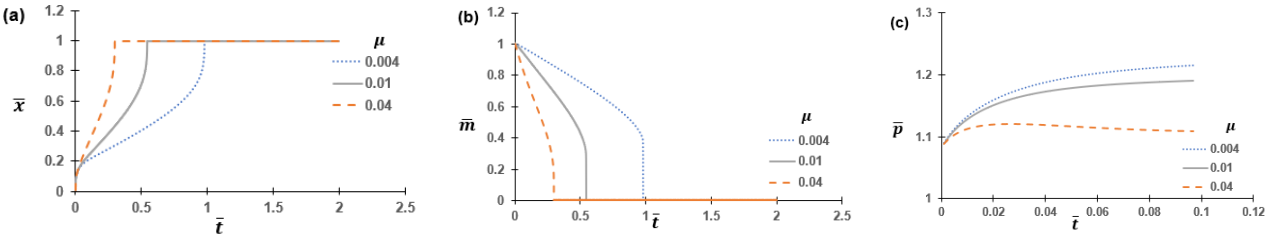

Figure 10. Parametric study of the impact of the dynamic viscosity μ [N·s/m^2]: (**a**) Normalized liquid height; (**b**) Normalized air mass; (**c**) Normalized air pressure. Other parameters are fixed, the diffusivity $D_dK_H = 2 \times 10^{-8}$ [mol·s/kg], surface tension $\sigma = 0.04$ N/m, and $U_0 = 1 \times 10^{-8}$.

Micromachines **2023**, *14*, x FOR PEER REVIEW 11 of 16

Figure 10. Parametric study of the impact of the dynamic viscosity μ [N·s/m^2]: (**a**) Normalized liquid height; (**b**) Normalized air mass; (**c**) Normalized air pressure. Other parameters are fixed, the diffusivity $D_dK_H = 2 \times 10^{-8}$ [mol·s/kg], surface tension $\sigma = 0.04$ N/m, and $U_0 = 1 \times 10^{-8}$.

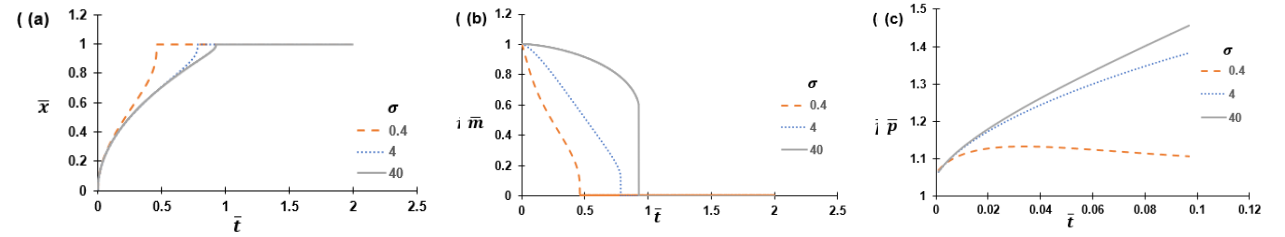

Figure 11. Parametric study of the impact of the surface tension σ [N/m]: (**a**) Normalized liquid height; (**b**) Normalized air mass; (**c**) Normalized air pressure. Other parameters are fixed, the diffusivity $D_dK_H = 2 \times 10^{-8}$ [mol·s/kg], dynamic viscosity $\mu = 0.4$ N/m, and $U_0 = 1 \times 10^{-8}$.

Figure 11. Parametric study of the impact of the surface tension σ [N/m]: (**a**) Normalized liquid height; (**b**) Normalized air mass; (**c**) Normalized air pressure. Other parameters are fixed, the diffusivity $D_dK_H = 2 \times 10^{-8}$ [mol·s/kg], dynamic viscosity $\mu = 0.4$ N/m, and $U_0 = 1 \times 10^{-8}$.

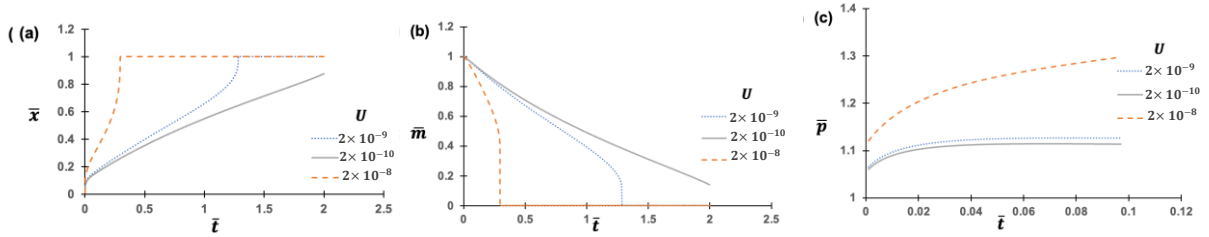

Figure 12. Parametric study of the impact of the initial potential (voltage) difference U_0: (**a**) Normalized liquid rise height; (**b**) Speed of normalized air mass reduction; (**c**) Normalized air pressure. Other parameters are fixed, the dynamic viscosity $\mu = 0.4$ N·s/m^2, the surface tension $\sigma = 0.04$ N/m, and the diffusivity $D_dK_H = 2 \times 10^{-8}$ [mol·s/kg].

Figure 12. Parametric study of the impact of the initial potential (voltage) difference U_0: (**a**) Normalized liquid rise height; (**b**) Speed of normalized air mass reduction; (**c**) Normalized air pressure. Other parameters are fixed, the dynamic viscosity $\mu = 0.4$ N·s/m^2, the surface tension $\sigma = 0.04$ N/m, and the diffusivity $D_dK_H = 2 \times 10^{-8}$ [mol·s/kg].

As the diffusivity of the trapped air into the PDMS pores decreases, the time required for the liquid to hit the top appears to increase (Figure 9a). This is aligned with basic physics, i.e., the higher the diffusivity, the faster the trapped air escapes. Similarly with higher diffusivity, the normalized mass ($\bar{m}$) decreases rapidly (Figure 9b) and trapped air pressure increases rapidly (Figure 9c).

In Figure 10, the complex relationship between the rate of liquid rise and the dynamic viscosity (μ). Equation (6) shows that $\frac{\delta \bar{x}}{\delta \bar{t}} \propto -\mu$. The second term of Equation (5) shows that $\frac{\delta \bar{m}}{\delta \bar{t}} \propto -\mu$. So, we can conclude $\frac{\delta \bar{x}}{\delta \bar{t}} \propto \mu$, which can be found in Figure 10a.

Figure 11 depicts a complex relationship between the rate of liquid rise and surface tension (σ). Equation (6) shows that $\frac{\delta \bar{x}}{\delta \bar{t}} \propto -\frac{1}{\sigma}$. This means that the rate of liquid rise decreases with increasing surface tension. Similarly, Equation (5) shows that $\frac{\delta \bar{m}}{\delta \bar{t}} \propto -\frac{1}{\sigma}$. Consequently, it becomes evident that α is inversely proportional to σ ($\alpha \propto \frac{1}{\sigma}$), β is also inversely proportional to σ ($\beta \propto \frac{1}{\sigma}$), and γ follows the same trend, being inversely proportional to σ ($\gamma \propto \frac{1}{\sigma}$). Furthermore, Equation (5) indicates that as γ increases, $\frac{\delta \bar{m}}{\delta \bar{t}}$ also increases while $\bar{m}$ decreases, and exponential forms of the equation [55] best fit the data. Upon examining the fitted weights, it was evident that the best fit was achieved with the expression $f(x) = \exp(c_1 x^{c_2})$ [55].

3.2.2. Comparisons among Different LEFs for Electrical Potential Dependent LEF

For diffusivity, surface tension, and dynamic viscosity, [55] explored various link functions, including linear, simple nonlinear, complex nonlinear, and exponential forms. Upon examining the fitted weights, it was evident that the best fit was achieved with the expression $f(x) = \exp(c_1 x^{c_2})$ [55].

To explain the impact of the different types of LEFs, two types of LEFs were considered to account for the effects of potential (voltage) difference and dielectric constants. The first was an exponential function of the form $f(x) = \exp(c_1 x^{c_2})$ and the second was a

increases. The second term of Equation (5) also shows that $\frac{\delta\overline{x}}{\delta\overline{t}} \propto -\overline{m}(\overline{t})$. Consequently, surface tension exerts both positive and negative influence on the rate of liquid rise. Specifically, as surface tension increases, the time required for the liquid to attain its maximum height increases.

Figure 12 gives another complex relationship between the rate of liquid rise and potential (voltage) difference (U). A potential difference existing between the lower surface of the PDMS and the upper surface of the liquid generates an attractive force between them. Consequently, U actively contributes to the rate of liquid rise. Following Equation (5), it becomes evident that $\frac{\delta\overline{x}}{\delta\overline{t}} \propto \gamma$, where $\gamma = \frac{U(h)d}{4\sigma h^2\cos(\theta)}$. As the value of $U(h)$ increases, the rate of liquid rise experiences a corresponding increase, leading to a faster attainment of the liquid's maximum height.

The link functions for diffusivity, surface tension, dynamic viscosity, and their impact on the rate of liquid rise and trapped-air mass reduction rate are derived from prior work [15]. These relationships, including the impact of potential (voltage) difference, are expressed through Equations (5) and (6), where α, β, and γ play key roles. The rate of liquid rise, $\left(\frac{\delta\overline{x}}{\delta\overline{t}}\right)$, is given by $\frac{\delta\overline{x}}{\delta\overline{t}} = \frac{1}{2\overline{x}(\overline{t})} - \frac{\alpha}{2}\left(\frac{\overline{m}(\overline{t})-1+\overline{x}(\overline{t})}{\overline{x}(\overline{t})(1-\overline{x}(\overline{t}))}\right) + \frac{\gamma}{\overline{x}(\overline{t})(1-\overline{x}(\overline{t}))^2}$, and the trapped-air mass reduction rate, $\frac{\delta\overline{m}}{\delta\overline{t}} = -\beta\left(1 + \frac{2h}{d}\left(1-\overline{x}(\overline{t})\right)\right)\left(\frac{\overline{m}(\overline{t})-1+\overline{x}(\overline{t})}{(1-\overline{x}(\overline{t}))}\right)$ where, $\alpha = \frac{P(0)d}{2\sigma_0\mathcal{L}_\sigma\cos(\theta)}$, $\beta = \frac{3\mu_0\mathcal{L}_\mu(D_dK_H)_0\ \mathcal{L}_{DK}RTh}{d\sigma_0\mathcal{L}_\sigma(x)\cos(\theta)\ l_{cr}}$, and $\gamma = \frac{U_0\mathcal{L}_U d}{4\sigma_0\mathcal{L}_\sigma(x)h^2\cos(\theta)}$. Notably, these link functions are interrelated, as evidenced by Equations (5) and (6). They collectively influence the height of liquid rise, demonstrating the intricate connection between diffusivity, surface tension, dynamic viscosity, and their effects on liquid behavior.

3.2. Comparisons among Different LFs for Electric Potential-Dependent LF

For diffusivity, surface tension, and dynamic viscosity, [15] explored various link functions, including constant, linear, simple nonlinear, complex nonlinear, and exponential forms. Upon examining the final height vs. UV dose graph, it was evident that the best fit was achieved with the expression $\mathcal{L}(x) = \exp(c_1x^{c_2})$ [15].

To explain the impact of the different types of LFs, two types of LFs were considered to account for the effects of potential (voltage) difference and dielectric constants. The first was an exponential function of the form $\mathcal{L}_U(x) = \exp(c_1x^{c_2})$ and the second was a second-order polynomial function of the form $\mathcal{L}_U(x) = c_1x^2 + c_2x + c_3$.

Two different approaches were taken for the polynomial LF; in the first, the free parameters for all four link functions were found using the Bayesian evolution, and in the second, the free parameters for $\mathcal{L}_U$ were kept constant, and parameters for the other three link functions were found. Using this method, we obtained four predictions for each experimental case after training the model for five epochs. The Mean Absolute Percentage Error (MAE) for each case was obtained (Figure 13), which showed that the polynomial LF where all the free parameters were found using the Bayesian evolution was the most accurate in predicting the sudden jump phenomenon.

The two best prediction results were from two cases of the polynomial LF with 26.39% and 13.10% MAE after training the model for five epochs. Therefore, the prediction result of the two was compared (Figure 14a,b). Figure 14b depicts the prediction results with the second-order polynomial LF with an increasing trend, which shows the sudden jump occurred at the same UV dose, which contradicts the experimental data. Conversely, Figure 14a (the decreasing trend of $\mathcal{L}_U$) clearly captures the trend followed by the sudden jump. Based on the result of Figure 14, the best prediction was obtained using a second-order polynomial LF with decreasing trend of $\mathcal{L}_U$.

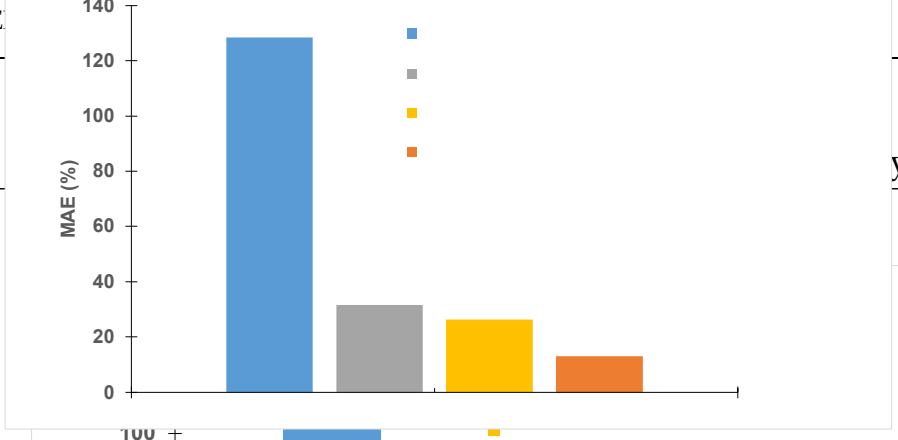

Figure 13. MAE of four cases of LF considered: No LF to account for voltage and dielectric constant, considering an exponential LF, and second-order polynomial LF with increasing and reducing trend.

The two best prediction results were from two cases of the polynomial LF with 26.39% and 13.10% MAE after training the model for five epochs. Therefore, the prediction result of the two was compared (Figure 14a,b). Figure 14b depicts the prediction results with the second-order polynomial LF with an increasing trend, which shows the sudden jump occurred at the same UV dose, which contradicts the experimental data. Conversely, Figure 14a (the decreasing trend of $\mathcal{L}_U$) clearly captures the trend followed by the sudden

Figure 13. MAE of four cases of LF considered: No LF to account for voltage and dielectric constant, considering an exponential LF, and second-order polynomial LF with increasing and reducing trend.

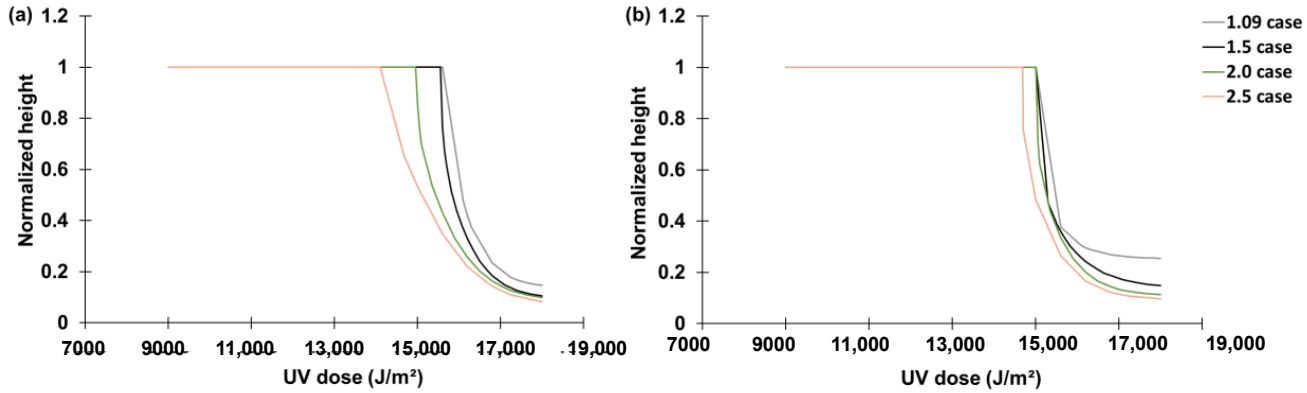

Figure 14. Comparison between (**a**) decreasing and (**b**) increasing trends of the electric potential link function $\mathcal{L}_U$.

Figure 14. Comparison between (**a**) decreasing and (**b**) increasing trends of the electric potential link function $\mathcal{L}_U$.

3.3. Remarks on the Difference from Statistical Learning

3.3. Remarks on the Difference from Statistical Learning

The proposed hybrid intelligence approach is more general than the statistical approach. As shown in Figure 15, the hybrid intelligence systematically explores the diverse candidates of input-parameter pairs $x \rightarrow y$ where $x \in$ {UV dose, mass flux rate, maximum height of nano-gratings} and $y \in$ {diffusivity, viscosity, surface tension, electric potential} in pursuit of the most plausible rule shapes. Due to observational and technological limits, y are scarce, rendering direct statistical fitting infeasible. To some extent, the internal parameters (y) can be regarded as latent variables in the "encoder" ML methods [19–21] (Figure 15). Figure 15f–h show preliminary investigations about how bad-performing rule shapes are rejected during the learning.

The proposed hybrid intelligence approach is more general than the statistical approach. As shown in Figure 15, the hybrid intelligence systematically explores the diverse candidates of input-parameter pairs $x \rightarrow y$ where $x \in$ {UV dose, mass flux rate, maximum height of nano-gratings} and $y \in$ {diffusivity, viscosity, surface tension, electric potential} in pursuit of the most plausible rule shapes. Due to observational and technological limits, y are scarce, rendering direct statistical fitting infeasible. To some extent, the internal parameters (y) can be regarded as latent variables in the "encoder" ML methods [19–21] (Figure 15). Figure 15f–h show preliminary investigations about how bad-performing rule shapes are rejected during the learning.

Figure 14. Comparison between (**a**) decreasing and (**b**) increasing trends of the electric potential link function $\mathcal{L}_U$.

3.3. Remarks on the Difference from Statistical Learning

The proposed hybrid intelligence approach is more general than th approach. As shown in Figure 15, the hybrid intelligence systematically e diverse candidates of input-parameter pairs $x \rightarrow y$ where $x \in$ {UV dose, ma maximum height of nano-gratings} and $y \in$ {diffusivity, viscosity, surfa electric potential} in pursuit of the most plausible rule shapes. Due to observ

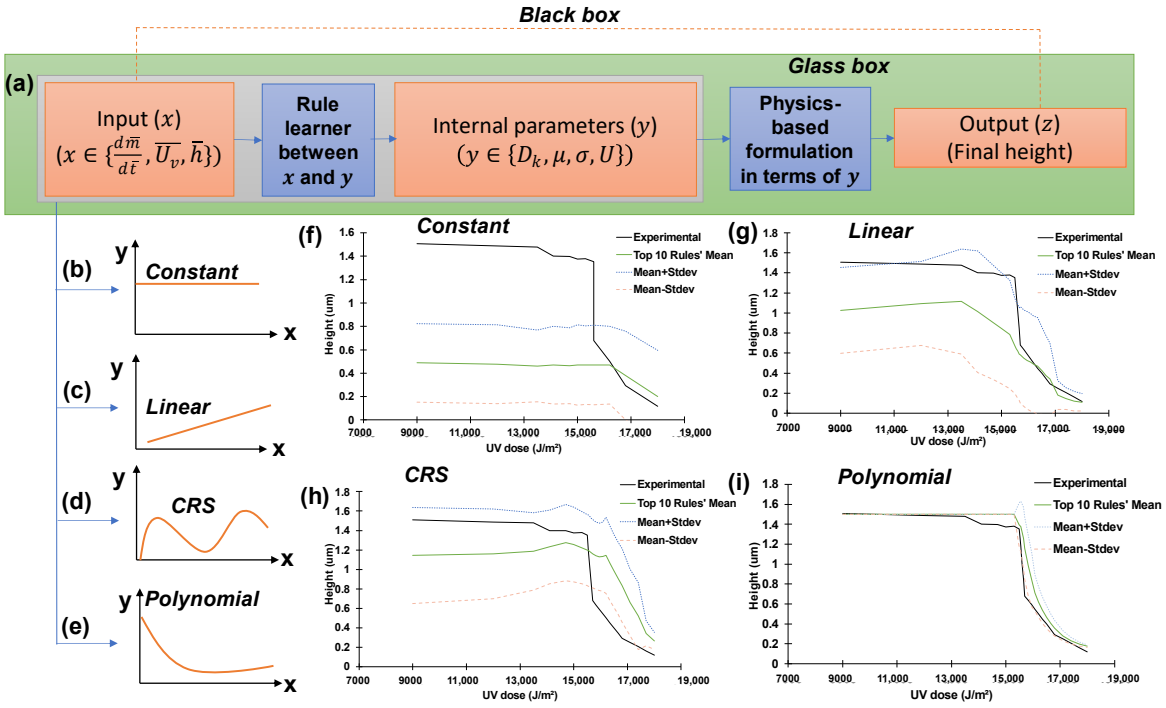

Figure 15. Illustration of the three global stages of the rule learning with diverse candidates for the hidden rules regarding important parameters ($y \in \{D_k, \mu, \sigma, U\}$) in terms of descriptive variables ($x \in \{\frac{d\bar{m}}{d\bar{t}}, \overline{U_v}, \bar{h}\}$): (**a**) Overall learning framework (glass-box)—this step represents the entire process starting with input (experimental data and an assumed link function), moving to internal parameters, and ultimately resulting in an output (i.e., the final height attained by the liquid). The red dotted lines show a black-box approach that takes input (x) and produces output (z), without any understanding of underlying principles; (**b**) Constant model-based rule; (**c**) Linear model-based rule; (**d**) Complex nonlinear curve-based rule that can be learned by the cubic regression splines (CRS); (**e**) 2nd-order polynomial model-based rule; (**f**–**i**) Examples of the best-so-far predictions that use the constant model-based rules (**f**), linear model-based rules (**g**), CRS model-based rules (**h**) exhibiting poor performance, and the best-so-far prediction using 2nd-order polynomial model-based rules (**i**).

4. Conclusions

This paper combines human insights with the searching power of machine learning to uncover hidden rules, collectively known as hybrid intelligence. This approach helped us understand the rules that explain the physical phenomena of a sudden jump in nanograting dynamic viscosity, diffusivity, and surface tension were previously recognized as the underlying physical phenomena explaining this occurrence. However, experimental data revealed the existence of a phenomenon that required an explanation for the correlation between the height of the PDMS mold and the final liquid height, which was unaddressed in prior research. Our hybrid intelligence approach allowed us to identify a potential (voltage) difference-dependent force that could fully elucidate the relationship between the mold's height and the final height reached, thereby explaining the phenomenon, irrespective of the PDMS mold's height.

Author Contributions: Conceptualization, I.H.C.; methodology, I.H.C. and A.C.; software, A.C. and I.H.C. All authors have read and agreed to the published version of the manuscript.

Funding: This work was supported by the National Science Foundation (NSF) under the grants OAC-1931380 (in part, I.H.C. and A.C.) and CMMI-2129796 (in part, A.C. and I.H.C.). The computational simulation reported in this paper is partially supported by the high-performance computing equipment at Iowa State University, some of which have been purchased through funding provided by the NSF CNS-2018594.

Data Availability Statement: All experimental data are available upon request to the corresponding author.

Conflicts of Interest: The authors declare no conflict of interest.

References

1. Bandara, C.D.; Singh, S.; Afara, I.O.; Wolff, A.; Tesfamichael, T.; Ostrikov, K.; Oloyede, A. Bactericidal Effects of Natural Nanotopography of Dragonfly Wing on Escherichia Coli. *ACS Appl. Mater. Interfaces* **2017**, *9*, 6746–6760. [CrossRef]
2. Siddique, R.H.; Gomard, G.; Hölscher, H. The Role of Random Nanostructures for the Omnidirectional Anti-Reflection Properties of the Glasswing Butterfly. *Nat. Commun.* **2015**, *6*, 6909. [CrossRef]
3. Tadepalli, S.; Slocik, J.M.; Gupta, M.K.; Naik, R.R.; Singamaneni, S. Bio-Optics and Bio-Inspired Optical Materials. *Chem. Rev.* **2017**, *117*, 12705–12763. [CrossRef]
4. Zhou, H.; Xu, J.; Liu, X.; Zhang, H.; Wang, D.; Chen, Z.; Zhang, D.; Fan, T. Bio-Inspired Photonic Materials: Prototypes and Structural Effect Designs for Applications in Solar Energy Manipulation. *Adv. Funct. Mater.* **2018**, *28*, 1705309. [CrossRef]
5. Lee, Y.; Bae, S.-I.; Eom, J.; Suh, H.-C.; Jeong, K.H. Antireflective Glass Nanoholes on Optical Lenses. *Opt. Express* **2018**, *26*, 14786. [CrossRef]
6. Li, Q.; Ji, M.G.; Kim, J. Grayscale nanopixel printing at sub-10-nanometer vertical resolution via light-controlled nanocapillarity. *ACS Nano* **2020**, *14*, 6058–6066. [CrossRef]
7. Phan, V.N.; Nguyen, N.T.; Yang, C.; Joseph, P.; Djeghlaf, L.; Bourrier, D.; Gue, A.M. Capillary Filling in Closed End Nanochannels. *Langmuir* **2010**, *26*, 13251–13255. [CrossRef]
8. Kolliopoulos, P.K.; Jochem, K.S.; Lade, R.K., Jr.; Francis, L.F.; Kumar, S. Capillary Flow with Evaporation in Open Rectangular Microchannels. *Langmuir* **2019**, *35*, 8131–8143. [CrossRef] [PubMed]
9. Zhang, F.; Zhou, X. General Exotic Capillary Tubes. *J. Fluid Mech.* **2019**, *885*, A1. [CrossRef]
10. Zhang, F.; Zhou, X. Capillary Surfaces in and around Exotic Cylinders with Application to Stability Analysis. *J. Fluid Mech.* **2020**, *882*, A28. [CrossRef]
11. Klinkenberg, L.J. The Permeability of Porous Media to Liquids and Gases. In *Drilling and Production Practice*; API-41-200; American Petroleum Institute: New York, NY, USA, 1941; pp. 200–213.
12. Wu, Y.S.; Pruess, K.; Persoff, P. *Steady and Transient Analytical Solutions for Gas Flow in Porous Media with Klinkenberg Effects*; LBNL-39499, UC-1240; Lawrence Berkeley National Laboratory: Berkeley, CA, USA, 1996.
13. Markov, P.; Rodionov, S. Numerical Simulation Using Finite-Difference Schemes with Continuous Symmetries for Processes of Gas Flow in Porous Media. *Computation* **2019**, *7*, 45. [CrossRef]
14. Pavan, V.; Oxarango, L. A New Momentum Equation for Gas Flow in Porous Media: The Klinkenberg Effect Seen through the Kinetic Theory. *J. Stat. Phys.* **2007**, *126*, 355–389. [CrossRef]
15. Cho, I.; Ji, M.G.; Kim, J. Pursuit of hidden rules behind the irregularity of nano capillary lithography by hybrid intelligence. *Sci Rep.* **2023**, *13*, 13649. [CrossRef]
16. Tanaka, G.; Yamane, T.; Héroux, J.; Nakane, R.; Kanazawa, N.; Takeda, S.; Numata, H.; Nakano, D.; Hirose, A. Recent advances in physical reservoir computing: A review. *Neural Netw.* **2019**, *115*, 100–123. [CrossRef] [PubMed]
17. Hochreiter, S.; Schmidhuber, J. Long short-term memory. *Neural Comput.* **1997**, *9*, 1735–1780. [CrossRef]
18. Gers, F.A.; Schmidhuber, J.; Cummins, F. Learning to forget: Continual prediction with LSTM. *Neural Comput.* **2000**, *12*, 2451–2471. [CrossRef]
19. Karpatne, A.; Atluri, G.; Faghmous, J.H.; Steinbach, M.; Banerjee, A.; Ganguly, A.; Shekhar, S.; Samatova, N.; Kumar, V. Theory-Guided Data Science: A New Paradigm for Scientific Discovery from Data. *IEEE Trans. Knowl. Data Eng.* **2017**, *29*, 2318–2331. [CrossRef]
20. Raissi, M.; Yazdani, A.; Karniadakis, G.E. Hidden fluid mechanics: Learning velocity and pressure fields from flow visualizations. *Science* **2020**, *367*, 1026–1030. [CrossRef] [PubMed]
21. Champion, K.; Lusch, B.; Kutz, J.N.; Brunton, S.L. Data-driven discovery of coordinates and governing equations. *Proc. Natl. Acad. Sci. USA* **2019**, *116*, 22445–22451. [CrossRef]
22. Schaschke, C. *Fluid Mechanics Worked Examples for Engineers*; Institution of Chemical Engineers: Rugby, UK, 1998; pp. 84–87.
23. Yang, Q.; Li, Q.; Tian, H.; Li, X.; Shao, J.; Chen, X.; Xu, F. Deformation Hysteresis of Electrohydrodynamic Patterning on a Thin Polymer Film. *ACS Appl. Mater. Interfaces* **2016**, *8*, 17668–17675. [CrossRef]
24. Cho, I.; Li, Q.; Biswas, R.; Kim, J. A Framework for Glass-Box Physics Rule Learner and Its Application to Nanoscale Phenomena. *Nat. Commun. Phys.* **2020**, *3*, 78. [CrossRef]
25. Cho, I.; Yeom, S.; Sarkar, T.; Oh, T. Unraveling Hidden Rules Behind the Wet-To-Dry Transition of Bubble Array by Glass-Box Physics Rule Learner. *Nat. Sci. Rep.* **2022**, *12*, 3191. [CrossRef] [PubMed]
26. Cho, I. A Framework for Self-Evolving Computational Material Models Inspired by Deep Learning. *Int. J. Numer. Methods Eng.* **2019**, *120*, 1202–1226. [CrossRef]

27. Bazroun, M.; Yang, Y.; Cho, I. Flexible and Interpretable Generalization of Self-Evolving Computational Materials Framework. *Comput. Struct.* **2021**, *260*, 106706. [CrossRef]
28. Cho, I. Gauss Curvature-Based Unique Signatures of Individual Large Earthquakes and Its Implications for Customized Data-Driven Prediction. *Nat. Sci. Rep.* **2022**, *12*, 8669. [CrossRef] [PubMed]